

Entropic Lattice Boltzmann Method for Moving and Deforming Geometries in Three Dimensions

B. Dorschner, Shyam S. Chikatamarla, and Ilya Karlin*

*Aerothermochemistry and Combustion Systems Lab,
Department of Mechanical and Process Engineering,
ETH Zurich, CH-8092 Zurich, Switzerland*

(Dated: October 3, 2018)

Entropic lattice Boltzmann methods have been developed to alleviate intrinsic stability issues of lattice Boltzmann models for under-resolved simulations. Its reliability in combination with moving objects was established for various laminar benchmark flows in two dimensions in our previous work Dorschner et al. [11] as well as for three dimensional one-way coupled simulations of engine-type geometries in Dorschner et al. [12] for flat moving walls. The present contribution aims to fully exploit the advantages of entropic lattice Boltzmann models in terms of stability and accuracy and extends the methodology to three-dimensional cases including two-way coupling between fluid and structure, turbulence and deformable meshes. To cover this wide range of applications, the classical benchmark of a sedimenting sphere is chosen first to validate the general two-way coupling algorithm. Increasing the complexity, we subsequently consider the simulation of a plunging SD7003 airfoil at a Reynolds number of $Re = 40000$ and finally, to access the model's performance for deforming meshes, we conduct a two-way coupled simulation of a self-propelled anguilliform swimmer. These simulations confirm the viability of the new fluid-structure interaction lattice Boltzmann algorithm to simulate flows of engineering relevance.

I. INTRODUCTION

Flows induced by complex and moving geometries are of paramount interest in many fields ranging from industrial applications for the optimization of internal combustion engines, turbines, etc., to flows in the field of bio-fluidmechanics in order to enhance our basic understanding of the propulsion mechanisms of animals, the flow through the cardiovascular system and many more (see, e.g., De Tullio et al. [10], Howell et al. [22], Kern and Koumoutsakos [27], Randles [43], Schmitt et al. [44]). Besides the valuable insight from experimental studies, light may be shed on these complex mechanisms through numerical simulations. Thus, accuracy, robustness and efficiency of the numerical treatment is crucial.

In this context, the lattice Boltzmann method (LBM) gains increasing attention due to its accuracy and reliability in various regimes including turbulence, thermal flows, compressible flows, micro flows, porous media and multiphase flows among many others (see Ansumali et al. [2], Bösch et al. [5], Frapolli et al. [16, 17], Mazloomi et al. [36], Mendoza et al. [38]). The LBM originates from kinetic theory and describes the flow in terms of discretized particle distribution functions (populations) $f_i(\mathbf{x}, t)$ associated with a set of discrete velocities $\mathbf{c}_i, i = 1, \dots, Q$, where the dynamics of the populations are constructed to recover the desired macroscopic equations in the hydrodynamic limit. Efficiency is achieved by organizing the discrete velocities into a regular lattice, resulting in a stream-and-collide algorithm with exact propagation and spatially local non-linearity implemented through the collision operator. The first realization, which made a practical connection of LBM to fluid dynamics was the well known lattice Bhatnagar-Gross-Krook (LBGK) model. The LBGK model remains popular due to its simplicity and numerical efficiency. Despite these attractive properties, the LBM was not competitive for long due to the lack of

* karlin@lav.mavt.ethz.ch

numerical stability and accurate boundary conditions in the simulation of high Reynolds number flows. This promoted the development of various models intended to resolve this issue, including explicit turbulence models in LBM formulation, multiple-relaxation time models (MRT) and others (see, e.g., Chen et al. [7], Geier et al. [18], Karlin et al. [25], Lallemand and Luo [28], Latt and Chopard [29]). Most notably, the entropic lattice Boltzmann method (Karlin et al. [25]), which, by introduction of a discrete entropy function H as the determining factor of the relaxation, features non-linear stability. In contrast to LBGK, the relaxation parameter is chosen adaptively at each point in space and time to locally ensure the discrete-time H-theorem. Consequently, an effective viscosity is prescribed by the second law of thermodynamics, which may both smoothen or enhance the flow field. Recently, the entropic concept was extended to multi-relaxation time models (KBC models), where the additional freedom of multiple relaxation parameters is used to keep the effective viscosity at its nominal value while retaining stability. Excellent performance of KBC models in terms of stability and accuracy for under-resolved simulations have been reported in the works of Bösch et al. [5], Dorschner et al. [12], Karlin et al. [26]. Due to its advantages, all simulations in the remainder of the paper are conducted using the KBC model.

In order to establish these entropy-based lattice Boltzmann models as a robust and predictive tool for complex engineering problems, the topic of boundary conditions needs to be addressed as its implementation is crucial for accuracy and stability of the entire simulation. Various proposals for flat, curved and moving boundaries can be found in the literature. Most popular for its simplicity is the bounce-back boundary condition, where the geometry is represented using a staircase approximation. For a more accurate representation of the geometry, common approaches use interpolation or extrapolation of the populations to account for the curvature of the object. However, spurious shocks for turbulence simulation at the boundary limit their usage to resolved and moderate Reynolds number flows. An interesting realization of the bounce-back can be found for a recent, so-called crystallographic LBM, in [40]. Another common approach for complex moving objects is the immersed boundary method (IBM), which was originally proposed by Peskin [42] for the simulation of blood flow. Notable in the LBM realm is the IBM procedure as introduced by Suzuki and Inamuro [45], which resolved the common issue of streamlines penetrating the object and more accurately satisfies the no-slip boundary condition.

In our recent contribution Dorschner et al. [11], we aimed to resolve these issues by employing Grad's approximation to impose the desired boundary conditions on the slow varying moments rather than the fluctuating population directly. In Dorschner et al. [11] excellent stability properties and second-order accuracy were reported. Further, this boundary condition was validated for various laminar benchmark simulations with stationary and moving walls in two-dimensions. In this paper we extend these models for moving objects in three dimension with a successively increasing level of complexity. First, we consider the classical two-way coupled benchmark simulation of a falling sphere under gravity to validate the boundary condition and the two-way coupling algorithm. The next level of complexity is a simulation of a plunging airfoil at $Re = 40000$ in the transitional regime, where we report a detailed comparison with experimental and numerical studies of McGowan et al. [37] and Visbal [48], respectively. Finally, the performance for deformable meshes is accessed on the example of a self-propelled anguilliform swimmer.

The paper is organized as follows: In section II, the entropic multi-relaxation time model is reviewed followed by a brief exposure of the boundary conditions in section III. Subsequently, in section IV, we present our results for the simulation of the sedimenting sphere, the plunging airfoil and the anguilliform swimmer. Finally, concluding remarks are given in section V.

II. ENTROPIC MULTI-RELAXATION TIME LATTICE BOLTZMANN MODEL - KBC MODEL

The population $f_i(\mathbf{x}, t)$ is evolved in accordance with the discrete kinetic equation

$$f_i(\mathbf{x} + \mathbf{c}_i, t + 1) = f'_i = (1 - \beta)f_i(\mathbf{x}, t) + \beta f_i^{\text{mirr}}(\mathbf{x}, t), \quad (1)$$

where the streaming step is prescribed by the left-hand side and the post-collision state f'_i is given on the right-hand side by a convex-linear combination of $f_i(\mathbf{x}, t)$ and the mirror state $f_i^{\text{mirr}}(\mathbf{x}, t)$. Various lattice Boltzmann schemes differ in the way the mirror state is constructed. The KBC model as employed in this paper represents the population f_i in its natural moment basis and partitions it into three parts as

$$f_i = k_i + s_i + h_i, \quad (2)$$

where the kinematic part k_i depends only on the locally conserved moments. The shear part is denoted by s_i and includes the deviatoric stress tensor. All remaining higher-order moments not included in k_i or s_i are lumped into h_i . The mirror state, in Eq. (1), can now be expressed as

$$f_i^{\text{mirr}} = k_i + (2s_i^{\text{eq}} - s_i) + ((1 - \gamma)h_i + \gamma h_i^{\text{eq}}), \quad (3)$$

where s_i^{eq} and h_i^{eq} denote s_i and h_i evaluated at equilibrium and the parameter γ quantifies the relaxation rate of the higher-order moments.

In the athermal case, the equilibrium populations f_i^{eq} are obtained by minimization of the discrete entropy function H subject to local mass and momentum conservation,

$$\min \left\{ H(f) = \sum_i f_i \ln \left(\frac{f_i}{W_i} \right) \right\}, \quad \text{s.t.} \sum_i \{1, \mathbf{c}_i\} f_i = \{\rho, \mathbf{j}\}, \quad (4)$$

where the lattice-specific weights are denoted by W_i . In this paper the standard three-dimensional $D3Q27$ lattice with a speed of sound of $c_s = 1/\sqrt{3}$ is used for all computations, where D and Q are the dimensionality and the number of discrete velocities, respectively. The exact solution to the minimization problem can be found in Ansumali et al. [1] (see also Bösch et al. [5] for a detailed discussion).

The Chapman-Enskog analysis applied to this system yields the Navier-Stokes equations with the shear viscosity ν and the bulk viscosity ξ as

$$\nu = c_s^2 \left(\frac{1}{2\beta} - \frac{1}{2} \right), \quad \xi = c_s^2 \left(\frac{1}{\gamma\beta} - \frac{1}{2} \right). \quad (5)$$

As for any MRT model trying to increase stability, the KBC model exploits the fact that the higher-order moments may be relaxed independently without affecting the hydrodynamic limit. However, unlike in the conventional MRT approach, the relaxation parameter γ in the KBC model is not a constant tuning parameter but is rather computed locally in every time step and at every grid point by minimizing the discrete entropy function in the post-collision state f'_i . The minimization results in the following equation for the stabilizer γ :

$$\sum_i \Delta h_i \ln \left[1 + \frac{(1 - \beta\gamma)\Delta h_i - (2\beta - 1)\Delta s_i}{f_i^{\text{eq}}} \right] = 0, \quad (6)$$

where $\Delta s_i = s_i - s_i^{\text{eq}}$ and $\Delta h_i = h_i - h_i^{\text{eq}}$. Moreover, an analytic approximation for the stabilizer γ may be obtained by expansion of Eq. (6) to the first non-vanishing order of $\Delta s_i/f_i^{\text{eq}}$ and $\Delta h_i/f_i^{\text{eq}}$ as

$$\gamma = \frac{1}{\beta} - \left(2 - \frac{1}{\beta} \right) \frac{\langle \Delta s | \Delta h \rangle}{\langle \Delta h | \Delta h \rangle}, \quad (7)$$

where the entropic scalar product $\langle X|Y \rangle = \sum_i (X_i Y_i / f_i^{\text{eq}})$ is introduced to ease notation. The accuracy of this approximation has proven to be sufficient for all simulations reported in this paper. For an in-depth discussion on the entropic multi-relaxation time models, the reader is referred to Bösch et al. [5].

III. WALL-BOUNDARY CONDITIONS

We here aim at extending the capabilities of KBC models to an accurate implementation of moving and deformable objects. Thus, the boundary conditions as detailed in Dorschner et al. [11] are briefly summarized.

In order to complete the streaming step in the LB algorithm, the set of populations \bar{D} advected from a solid node \mathbf{x}_s to a fluid boundary node \mathbf{x}_b are unknown and require to be specified in accordance with the desired boundary conditions. In Dorschner et al. [11] we proposed to approximate these "missing" populations by an analog of Grad's distribution function. This results in a parametrization of the distribution in terms of relevant moments, where not only locally conserved but also other pertinent moments may be taken into account. It is worth noting that this is in line with the notion of minimal entropy as used in bulk for the KBC model as the Grad distribution may analogously be derived using minimum entropy or quasi-equilibrium considerations as discussed in Gorban and Karlin [19]. In the athermal case as considered in this paper, it suffices to include the locally conserved quantities along with the pressure tensor $\mathbf{\Pi}$. Explicitly, the Grad distribution with those contributions reads

$$f_i^*(\rho, \mathbf{u}, \mathbf{\Pi}) = W_i \left[\rho + \frac{\rho}{c_s^2} \mathbf{c}_i \cdot \mathbf{u} + \frac{1}{2c_s^4} (\mathbf{\Pi} - \rho c_s^2 \mathbf{I}) : (\mathbf{c}_i \otimes \mathbf{c}_i - c_s^2 \mathbf{I}) \right], \quad (8)$$

where the pressure tensor is approximated as

$$\mathbf{\Pi} = \mathbf{\Pi}^{\text{eq}} + \mathbf{\Pi}^{\text{neq}}, \quad (9)$$

with

$$\mathbf{\Pi}^{\text{eq}} = \rho c_s^2 \mathbf{I} + \rho \mathbf{u} \otimes \mathbf{u}, \quad (10)$$

$$\mathbf{\Pi}^{\text{neq}} = -\frac{\rho c_s^2}{2\beta} (\nabla \mathbf{u} + \nabla \mathbf{u}^\dagger). \quad (11)$$

The full specification of Grad's distribution requires the density ρ , the velocity \mathbf{u} and the pressure tensor to be prescribed. For this purpose, the concept of target values is introduced. The momentum exerted by the object is accounted for by specifying an appropriate target velocity \mathbf{u}_{tgt} at \mathbf{x}_b , which may be obtained by an interpolation involving the wall velocity $\mathbf{u}_{w,i} = \mathbf{u}(\mathbf{x}_{w,i}, t)$ at the intersection point $\mathbf{x}_{w,i}$ with the object along the velocity vector \mathbf{c}_i and the velocities $\mathbf{u}_{f,i} = \mathbf{u}(\mathbf{x}_{f,i}, t)$ at the adjacent fluid nodes $\mathbf{x}_{f,i} = \mathbf{x}_b + \mathbf{c}_i \delta_t$ for $i \in \bar{D}$. Using an averaged linear interpolation for the target velocity yields

$$\mathbf{u}_{\text{tgt}} = \frac{1}{n_{\bar{D}}} \sum_{i \in \bar{D}} \frac{q_i \mathbf{u}_{f,i} + \mathbf{u}_{w,i}}{1 + q_i}, \quad (12)$$

where $n_{\bar{D}}$ is the number of unknown populations and $q_i = \|\mathbf{x}_b - \mathbf{x}_{w,i}\| / \|\mathbf{c}_i\|$. The target density on the other hand has two contributions corresponding to the static and the dynamic part as

$$\rho_{\text{tgt}} = \rho_{\text{stat}} + \rho_{\text{dyn}} \quad (13)$$

with

$$\rho_{\text{stat}} = \sum_{i \in \bar{D}} f_i^{\text{bb}} + \sum_{i \notin \bar{D}} f_i, \quad (14)$$

$$\rho_{\text{dyn}} = \sum_{i \in \bar{D}} 6W_i \rho_0 \mathbf{c}_i \cdot \mathbf{u}_{w,i}, \quad (15)$$

where the static part ρ_{stat} is the implied density if one were to use the bounce-back boundary condition to ensure no mass flux through the boundary. The reflected population f_i^{bb} is defined as $f_i^{\text{bb}} = \tilde{f}_i$, where \tilde{f}_i is associated with the velocity vector $\tilde{\mathbf{c}}_i = -\mathbf{c}_i$. The dynamic part ρ_{dyn} accounts for the density alteration caused by the mass displacement by the moving body and may be derived by introducing a forcing term F_i , which is necessary for the displacement. The mass and momentum conservation $\sum_{i \in \bar{D}} F_i = 0$ and $\sum_{i \in \bar{D}} \mathbf{c}_i F_i = \rho \mathbf{u}_w$ directly lead to

$$F_i = 6W_i \rho \mathbf{c}_i \cdot \mathbf{u}_w \quad (16)$$

for the $D3Q27$ -lattice, where the summation over all unknown populations in \bar{D} yields the implied change in density for moving objects. Finally, the pressure tensor is prescribed by computing $\nabla \mathbf{u}$ using a finite difference scheme and the velocity values from the previous time step and evaluating Eqs. (10-11). Another aspect to be considered for moving objects is the reinitialization or refill of the lattice sites, which are uncovered as the objects passes by. For such nodes, we again employ the Grad distribution as given in Eq. (8) with the wall velocity and a local density average. The pressure tensor is evaluated in the same manner as for the boundary conditions.

These boundary conditions constitute the action of the object onto the fluid. On the other hand, for two-way coupled simulations, the feedback exerted from the fluid onto the object is accounted for by solving Newton's equations of motion and will be detailed in the corresponding section below.

IV. RESULTS AND DISCUSSION

A. Sedimenting sphere

As a first step to validate the proposed two-way coupled KBC algorithm, we consider the classical benchmark of a settling particle under gravity. For this purpose, we conduct two simulations. In the first simulation, we keep the sphere stationary and impose a mean flow in order to validate and compute the drag coefficient and the recirculation length for a Reynolds number of $\text{Re} = u_\infty D_s / \nu = 100$. The sphere is resolved with $D_s = 30$ grid points and the characteristic velocity $u_\infty = 0.01$ is given by the mean flow velocity. After the initial transient, the drag coefficient and the recirculation length are measured and the results are listed in Table (I) along with literature values. With a good agreement to all reference data, we perform a second simulation for which there is no mean flow velocity but instead the sphere is settling under gravity. When released in a quiescent fluid with density ρ_f , the sphere with density ρ_s accelerates towards

Table I: Flow past a sphere at $\text{Re} = 100$.

Contribution	C_d	L/D
Johnson and Patel [24]	1.1	0.88
Eitel-Amor et al. [14]	1.098	0.87
present	1.1	0.86

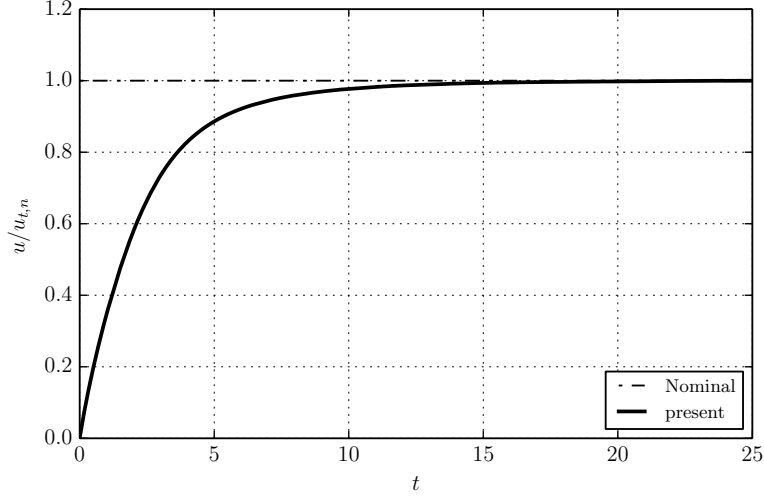


Figure 1: Temporal velocity evolution of a sedimenting sphere.

its terminal settling velocity u_t for which the gravitational force $F_g = \pi D_s^3 \rho_s g / 6$ is balanced by the buoyancy force $F_b = \pi D_s^3 \rho_f g / 6$ and the drag force $F_d = \rho_f u^2 \pi D_s^2 C_d / 8$. Establishing the force balance relates the density ratio to the terminal velocity as

$$\frac{\rho_s}{\rho_f} = 1 + \frac{3u_t^2 C_d}{4D_s g}, \quad (17)$$

where C_d is the drag coefficient. In this two-way coupled simulation, the feedback from the fluid onto the sphere is prescribed by Newton's equations for the particle motion as

$$\dot{\mathbf{x}}_s = \mathbf{u}_s, \quad (18)$$

$$\ddot{\mathbf{x}}_s = \frac{\mathbf{F}}{m_s} + \left(1 - \frac{\rho_f}{\rho_s}\right) \mathbf{g}, \quad (19)$$

$$(20)$$

which is solved by an Euler integration and the force \mathbf{F} is computed via the Galilean invariant momentum exchange method (see Wen et al. [49]). The evolution of the settling velocity is shown in Fig. (1) for an imposed drag coefficient from the stationary simulation and a nominal settling velocity of $u_{t,n} = 0.01$. After the initial acceleration, a terminal velocity of $u_t = 0.0100033$ is reached at $t = t_{lb} u_{t,n} / D = 25$ non-dimensional time units, which corresponds to less than 0.033% error. Thus, Galilean invariance is established between the stationary and the moving case and therefore validates the basic two-way coupling algorithm.

B. Plunging Airfoil

In this section, we leave the laminar flow regime and focus on the transitional flow past a plunging airfoil at a Reynolds number $\text{Re} = 40000$. Motivated to deepen our understanding of the complex physics relevant to small fliers, small unmanned air vehicles, micro air vehicles and alike, this setup was recently investigated experimentally and numerically in the works of McGowan

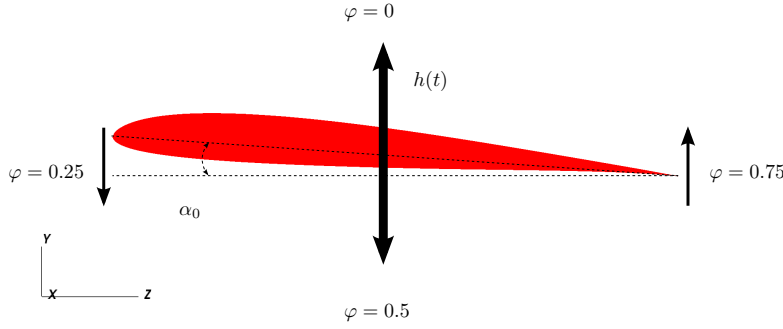


Figure 2: Schematic of a plunging airfoil.

et al. [37], Ou et al. [41], Visbal [48]. Analogous to small fliers, the flow is mainly characterized by the formation of dynamic-stall vortices on the leading edge due to the large induced angle of attack. The transitional flow regime is particularly demanding for turbulence models as a high-Reynolds number analysis may not be valid in the presence of both laminar and turbulent flow. This gives us the opportunity to test both the KBC model and the implementation of moving boundaries to its full extent. Notable is the recent study from Visbal [48] using an implicit Large-Eddy simulation (ILES, see, e.g., Margolin et al. [34], Margolin and Rider [35] for details and the rationale of ILES) with high-order compact schemes for the spatial derivatives needed to capture the transitional processes accurately and a Pade-type low-pass filter to gain stability.

In particular and as shown in Fig. (2), the flow past a plunging SD7003 airfoil with a static angle of attack $\alpha_0 = 4^\circ$ is considered in this contribution. The airfoil is resolved by $L = 400$ lattice points using two levels of block-refinement with a refinement ratio of two near the airfoil and a domain of $[10L \times 5L \times 0.2c]$ in the streamwise, lateral and spanwise direction, respectively. The grid refinement technique used within this context is detailed and validated in Dorschner et al. [13]. Same as in Visbal [48], a sinusoidal plunging motion of the airfoil is prescribed with a non-dimensional plunging amplitude of $h_0 = h_D/c = 0.05$ and a reduced frequency of $k = \pi f c / u_\infty = 3.93$ as

$$h(t) = h_0 \sin(2kF(t)) \quad (21)$$

where

$$F(t) = 1 - e^{-at}, \quad a = 4.6/2 \quad (22)$$

is an initial delay function to achieve a smooth transition from the resting airfoil to the plunging motion. This corresponds to an induced angle of attack $\alpha = 21.5^\circ$, which is sufficient for the formation of unsteady leading-edge separation and dynamic-stall-like vortices.

Capturing the main flow features occurring during the periodical motion of the airfoil, Fig. (3) shows four volume renderings of the instantaneous vorticity for phase angles of $\varphi = \{0, \frac{1}{4}, \frac{1}{2}, \frac{3}{4}\}$, corresponding to maximum upward displacement, maximum downward velocity, maximum downward displacement and maximum upward velocity, respectively (see also Fig. (2)). At the beginning of a new cycle, at a position of maximum upward displacement, the boundary layer near the leading-edge appears laminar and attached to the surface (see Fig. (3a)). At later times, caused by the downward acceleration, an emerging flow separation can be observed at the leading-edge (see Fig. (3b)). At bottom dead center (BDC), the flow is fully separated at the leading-edge on the upper surface of the airfoil, causing the formation of two coherent vortices (see Fig. (3c)). However, due to spanwise instabilities, these vortices break down into three dimensional, fine-scale turbulence during the subsequent upward acceleration (see Fig. (3d)).

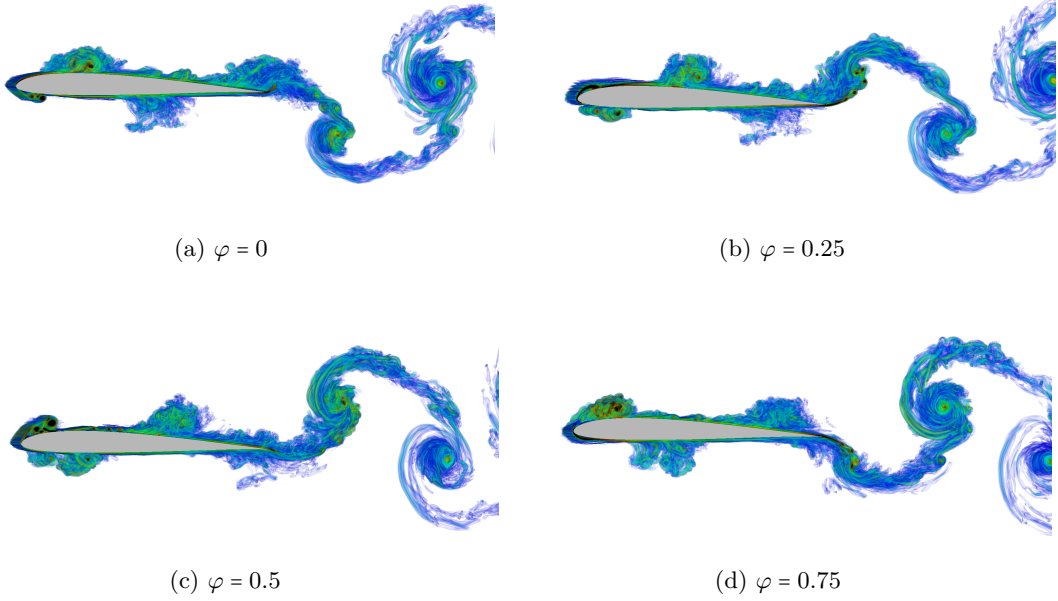


Figure 3: Volume rendering of vorticity for various phases of the plunging airfoil.

While diffusing and annihilating, these vortices propagate close to the airfoil surface during the following cycle. Note that due to the high frequency, a new pair of vortices is formed before the vortex pair of the previous cycle is shed from the trailing edge. Identical but less pronounced is the flow structure on the lower surface of the airfoil, where the large negative motion-induced angle of attack causes the formation of two coherent vortex structures, which subsequently break down into turbulence. Similar observations were reported by Visbal [48].

More quantitatively, in Fig. (4), we compare the phase-averaged velocity profiles in the near wake of the airfoil at $x/c = 1.5$ with the study of Visbal [48]. In total 25 cycles were computed and the first ten were neglected in the accumulation of statistics to avoid accounting for the initial transient. It is apparent that the main flow features are captured for both simulations and the agreement is good. The location of the minimum and maximum of the flow velocity agree well but differ slightly in terms of magnitude. The present simulation exhibits larger velocity magnitudes in comparison with the more smoothed ILES simulation. In addition, a comparison at a location further downstream at $x/c = 2$ with an experimental investigation using Particle Image Velocimetry (PIV), an immersed boundary method and the NASA-CFL3D code from the study of McGowan et al. [37] is shown in Fig. (5). It is apparent that due to the complexity of the problem all data have notable discrepancies but the agreement of the present study with the experiment is reasonable.

Finally, we compare the evolution of the aerodynamic forces for three selected cycles with Visbal [48] in Fig. (6). The lift coefficient C_L is dominated by the prescribed motion of the airfoil and has a large amplitude. On the other hand, the amplitude of the drag coefficient is much smaller but notably there is a net mean thrust corresponding to a mainly negative drag coefficient. The comparison with the ILES is excellent.

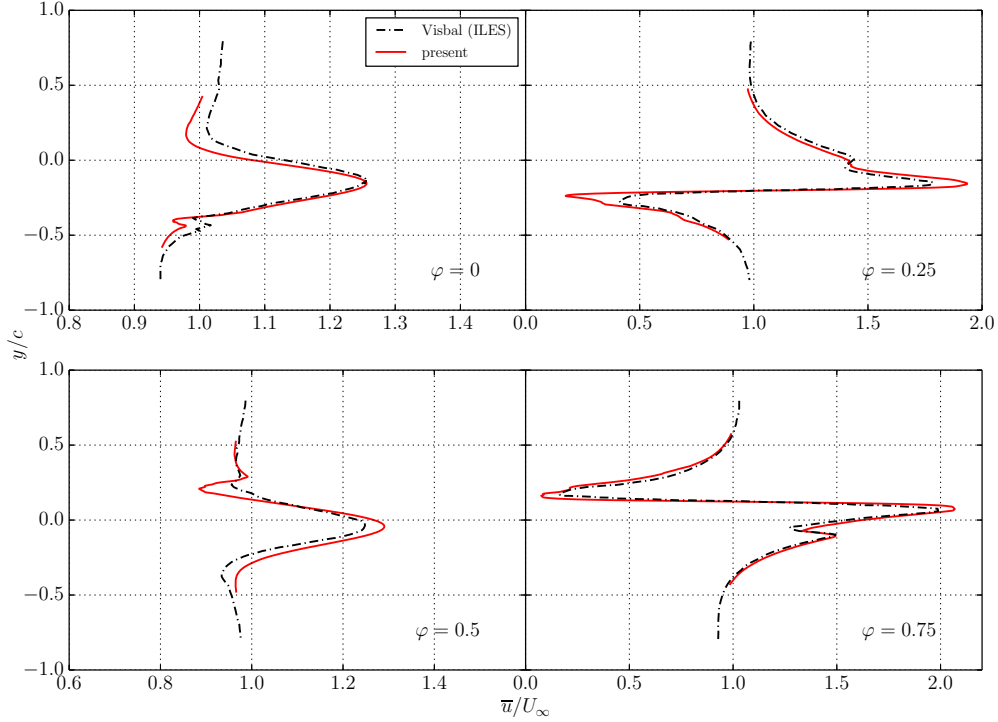


Figure 4: Phase-averaged velocity profiles for $x/D = 1.5$.

C. Anguilliform Swimmer

In the field of bio-fluidmechanics, the topic of aquatic animal propulsion mechanisms is much discussed among biologists, neuro-scientist as well as engineers trying to mimic these mechanisms to increase efficiency in technical applications (see, e.g., Ekeberg [15], Ijspeert and Kodjabachian [23], Tytell and Lauder [47]). However, due to the complex interaction between the fluid and the deformable body of the animal, fundamental questions regarding thrust generation and its relation to the kinematics of the swimmer's body, the efficiency and viscous effects remain controversial. In particular, investigations of the undulatory propulsion mechanisms of anguilliform fish (e.g.: *Anguilla anguilla*) started with the pioneering work of Gray [20]. In contrast to carangiform fish, anguilliform swimmers generate thrust by passing a transverse wave down their body and therefore utilizing, to a varying degree, the whole body for thrust generation and not just the tail. The hydrodynamics of aquatic locomotion for undulatory swimmers was studied for inviscid flow in the works of Cheng et al. [8], Hess and Videler [21], Lighthill [30, 31, 32, 33], Wu [50].

Simple algebraic models predict a reverse von Karman vortex street for optimized swimming performance, where the wake consists of a double row of single vortices when the ratio of the swimming speed and the body wave speed is less than one (Lighthill [31]).

On the experimental side, Particle Image Velocimetry (PIV) has proven itself as a valuable tool to quantify the flow field generated by the swimmer. The first visualization using two-dimensional PIV for freely swimming juvenile eel was reported by Müller et al. [39]. They found a linearly increasing flow velocity from head to tail, suggesting continuous thrust generation along the body. In the wake, they observed a double row of double vortices with little backward momentum, which is generated by a start-stop vortex shed from the tail and a separate vortex produced along the

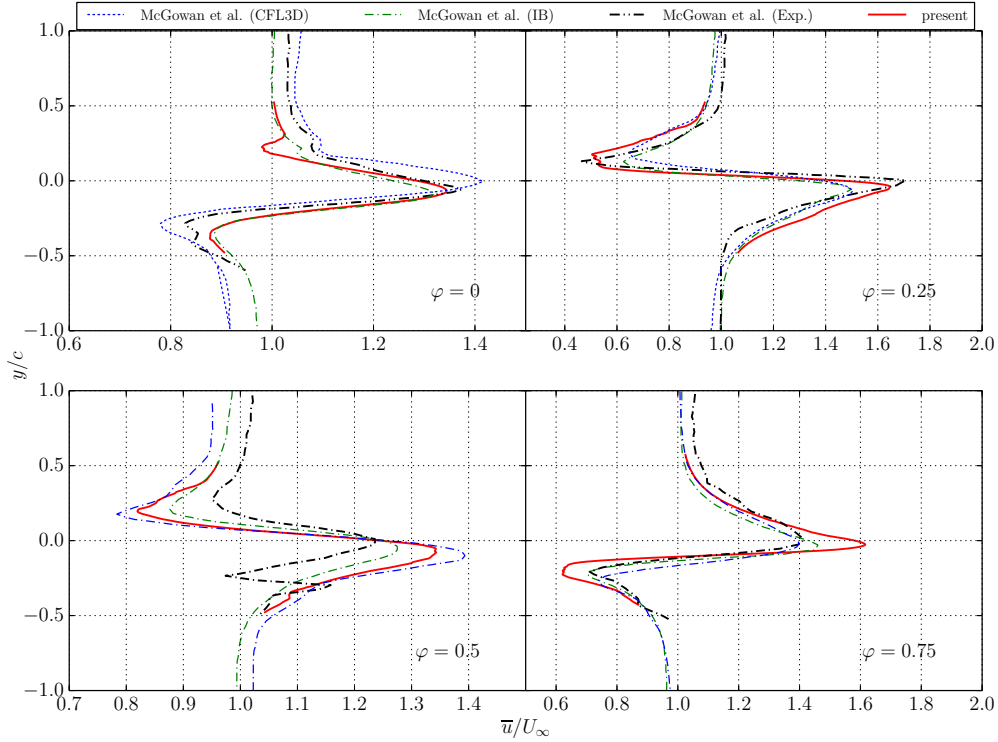


Figure 5: Phase-averaged velocity profiles for $x/D = 2$.

body, so-called proto-vortices, for each half tail-beat. They conjectured that the wake morphology is caused by a phase lag between the primary start-stop vortex and the body-generated circulation. Subsequent studies using high-resolution PIV were conducted by Tytell and Lauder [47]. Their results were, in general, similar to Müller et al. [39] but differences were noticed regarding the proto-vortices. Only a negligible phase lag with low vorticity was reported, resulting in a single, combined primary start-stop vortex per half tail-beat. The discrepancies were attributed to the lower PIV resolution and the seemingly accelerating eel in Müller et al. [39] compared to the steadily swimming fish in Tytell and Lauder [47]. In the work of Tytell and Lauder [47], they stated the following mechanism for the generation of the wake: A primary start-stop vortex is shed when the tail changes direction. Due to the acceleration of the tail from one side to the other, a low pressure region develops in the posterior part of the body, drawing fluid in the lateral direction, which is shed off the tail and stretches the primary vortex into an unstable shear layer which rolls up into two separate, co-rotating vortices, which they termed the secondary vortex. Thus, the primary vortex from one half tail beat and the secondary vortex from the subsequent comprise the boundaries of each lateral jet. Notable was the lack of any significant downstream flow for steady swimming as previously observed for carangiform fish and interpreted as thrust generation mechanism. This was further supported by the observation of only a slight upstream inclination of the lateral jets.

On the numerical front, only a few detailed studies may be found in literature (see, e.g., Borazjani and Sotiropoulos [3, 4], Carling et al. [6], Kern and Koumoutsakos [27]). The first two-dimensional viscous flow simulations of self-propelled anguilliform fish were reported in the work of Carling et al. [6]. In contrast to the experimentally observed wake morphology, these simulations indicated a single, large vortex ring wrapping around the eel, resulting in an upstream

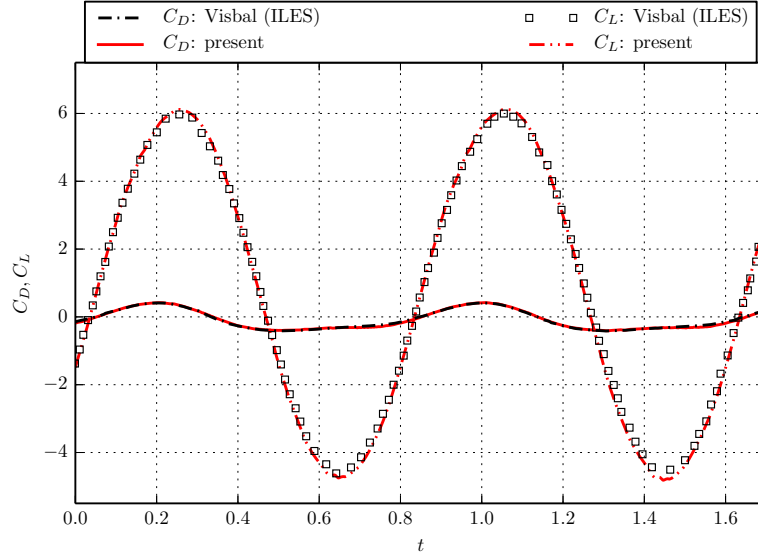


Figure 6: Evolution of lift and drag coefficient over three exemplary cycles of a plunging airfoil.

flow, where thrust is almost exclusively produced along the body and not the tail tip. Three dimensional simulations were recently conducted by Kern and Koumoutsakos [27] using the finite volume approach of the commercial software package STAR-CD with a first-order discretization in time and second-order in space. Apart from prescribing a reference motion of the fish, as proposed by Carling et al. [6], an evolutionary algorithm was employed to obtain the body motion as a result of optimizing for burst swimming speed and efficiency. Their results indicate that large amplitude tail undulation in combination with a straight anterior body produce most of the thrust at the tail and are optimal kinematics in the burst swimming mode. On the other hand, optimal kinematics for efficient swimming were obtained for an undulation of the entire body, where thrust is generated with half the body and not just the tail. For all swimming patterns, the wake morphology did not differ qualitatively and is in agreement with the experimental observations of Tytell and Lauder [47], exhibiting a double row of single vortex rings with lateral jets.

Despite the valuable contributions mentioned above, further quantitative analysis is needed for conclusive results. The ease of data extraction, its analysis and the precise control over the body's kinematics make numerical experiments useful for these studies. However, issues related to deformable meshes and the complex fluid-structure interaction are challenging for numerical solvers, thus explaining the sparsity of these simulations in literature. The KBC model on the other hand is a highly efficient approach, which allows for a simple implementation of complex, deformable bodies using Cartesian meshes and is therefore ideally suited for this type of problem. The moving wall boundary condition of Dorschner et al. [11] allows for non-body fitted meshed, which significantly reduces and simplifies the process of grid generation. This, combined with the superior stability of KBC models, the intrinsic parallelizability and efficiency of LBM make these the best available tools for DNS investigations of such complex flows. Therefore, as a first step to access the predictive capabilities of the proposed scheme, we conduct a simulation of a self-propelled anguilliform swimmer analogous to Kern and Koumoutsakos [27].

Geometrically, the body of the anguilliform swimmer with length L is modeled by spatially varying ellipsoidal cross sections as in Kern and Koumoutsakos [27] for which the half axes $w(s)$

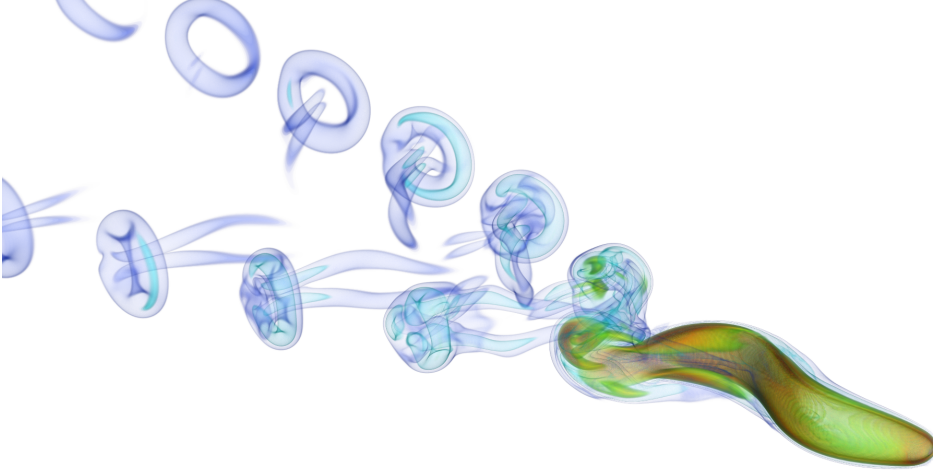


Figure 7: Volume rendering of vorticity of the swimmers wake, showing the typical double row vortex street.

and $h(s)$ are defined as analytical functions of the arc-length s as

$$w(s) = \begin{cases} \sqrt{2w_h s - s^2} & 0 \leq s < s_b, \\ w_h - (w_h - w_t) \left(\frac{s-s_b}{s_t-s_b} \right)^2 & s_b \leq s < s_t, \\ w_t \frac{L-s}{L-s_t} & s_t \leq s \leq L, \end{cases} \quad (23)$$

where $w_h = s_b = 0.04L$, $s_t = 0.95L$ and $w_t = 0.01L$. For the height $h(s)$ an elliptical curve is prescribed as

$$h(s) = b \sqrt{1 - \left(\frac{s-a}{a} \right)^2}, \quad (24)$$

where the half axes are given as $a = 0.51L$ and $b = 0.08L$. As proposed by Carling et al. [6], the swimmer undergoes a prescribed time-dependent lateral deformation of the body's center-line as

$$y(s, t) = 0.125\beta L \frac{s/L + 0.03125}{1.03125} \sin \left(2\pi \left(\frac{s}{L} - \frac{t}{T} \right) \right), \quad (25)$$

where T is the undulation period and β is an initial ramping function to assure a smooth transition from the initially resting body according to

$$\beta = \begin{cases} \frac{1-\cos(\pi t/T)}{2} & 0 \leq t \leq T, \\ 1 & t > T. \end{cases} \quad (26)$$

The feedback from the fluid onto the body is prescribed by Newton's equations as

$$m_s \ddot{\mathbf{x}}_s = \mathbf{F} \quad (27)$$

$$\frac{d\mathbf{I}_s \boldsymbol{\omega}_s}{dt} = \mathbf{M}, \quad (28)$$

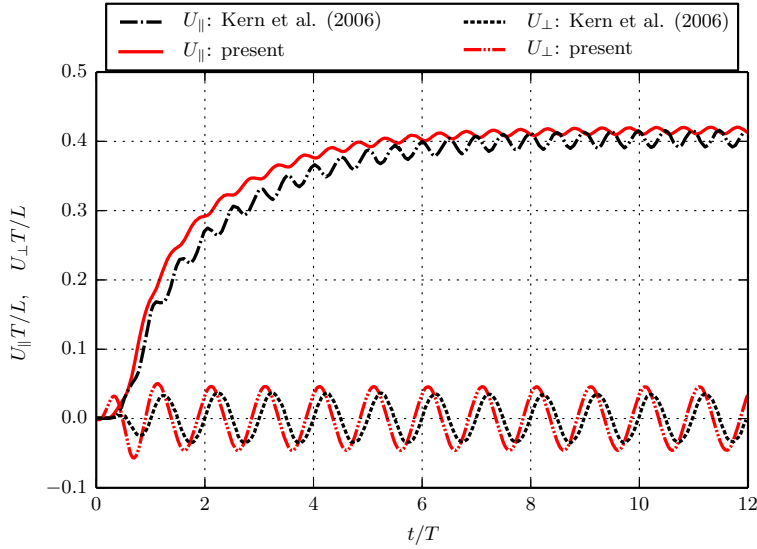


Figure 8: Temporal evolution of the forward velocity U_{\parallel} and lateral velocity U_{\perp} .

where m_s , \mathbf{I}_s , \mathbf{x}_s are the mass, the inertia tensor and the center of mass, respectively. The force and torque acting from the fluid onto the object are denoted by \mathbf{F} and \mathbf{M} , respectively. As in the work of Kern and Koumoutsakos [27], the complexity of the system is reduced by only considering the torque corresponding to the yaw. In the framework of the LB simulation, the geometrical model is represented as a triangulated surface composed of elliptical disks along the center-line. The center-line was decomposed into 150 segments, which has proven to be sufficient. This allows for a straightforward computation of all geometrical properties including the time derivative of the inertia tensor. The velocity at the intersection points, needed for the boundary conditions, was computed based on a finite-difference scheme and a barycentric interpolation for the given time-dependent deformation. As above, the equations of motion are solved using an Euler integration scheme. Higher-order integration schemes have been tested but marginal differences were observed due to the relatively small time step used. Further, no smoothing or low-pass filtering of the hydrodynamic forces were applied, unlike in Kern and Koumoutsakos [27].

The simulations are carried out with a uniform grid using a domain of $[8L \times 4L \times L]$, the swimmer is resolved by $L = 200$ lattice points and the undulation period is taken to be $T = 10^4$ lattice time steps. Same as in the reference, the Reynolds number is taken as $\text{Re} = (L^2/T)/\nu = 7142$.

A volume rendering of vorticity shows the wake of the swimmer in Fig. (7). In agreement with Kern and Koumoutsakos [27], Tytell [46], Tytell and Lauder [47], the wake consists of a double row of single vortices. Furthermore, we confirm the measurements from Tytell and Lauder [47] and observe a primary vortex being shed from the tail when it changes direction. The fluid drawn in lateral direction by the accelerating tail and the development of two separate co-rotating vortices as a result of an unstable shear layer roll-up can also be seen in Fig. (7).

Quantitatively, we compare the evolution of the forward and the lateral velocity of the swimmer in Fig. (8). Overall, the agreement is good. Minor, discrepancies are observed during acceleration but are attributed to different ramping functions used here, Eq. (26), and in Kern and Koumoutsakos [27]. The differences in the asymptotic forward and lateral velocity are within the range of expectation due to the different evolution algorithms. While Kern and Koumoutsakos [27] report an asymptotic forward velocity of $\bar{U}_{\parallel} = 0.4$ with an amplitude of 0.01, the present

simulation yields $\bar{U}_{\parallel} = 0.415$ with an amplitude of 0.005. The lateral velocity U_{\perp} has a zero mean for both the reference and the present simulation. An amplitude of 0.046 is measured in the present simulation whereas Kern and Koumoutsakos [27] measure 0.03. All simulations were checked for grid independence.

V. CONCLUSION

In this contribution we have presented a thorough study of the entropic multi-relaxation time model in combination with the Grad boundary condition for moving and deformable objects in three dimensions. After validation using the classical benchmark of a sedimenting sphere under gravity, the accuracy and robustness of the proposed method was accessed in the simulation of a plunging airfoil in the transitional regime. The comparison with literature revealed excellent agreement in all quantities including phase-averaged velocity profiles in the near wake region as well as the evolution of aerodynamic loads, important for realistic two-way coupled simulations. Finally, for deformable objects, the simulation of an anguilliform swimmer was considered and validated by comparison to the numerical investigations of Kern and Koumoutsakos [27]. These simulations together with the previous studies (Bösch et al. [5], Chikatamarla and Karlin [9], Dorschner et al. [12]) establish the predictive capabilities of KBC models for complex, moving and deforming objects, where a simple grid-convergence study is sufficient to assert their validity. The above simulations of complex flows, when viewed together with the efficiency of KBC models and the ease of implementing boundary conditions, demonstrate that the present method may be a viable alternative for engineering-related fluid dynamics.

ACKNOWLEDGMENTS

This work was supported by the European Research Council (ERC) Advanced Grant No. 291094-ELBM and the ETH-32-14-2 grant. The computational resources at the Swiss National Super Computing Center CSCS were provided under the grant s492 and s630.

-
- [1] S. Ansumali, I. V. Karlin, and H. C. Öttinger. Minimal entropic kinetic models for hydrodynamics. *Europhysics Letters*, 63(6):798–804, 2003.
 - [2] S. Ansumali, I. V. Karlin, C. E. Frouzakis, and K. B. Boulouchos. Entropic lattice Boltzmann method for microflows. *Physica A: Statistical Mechanics and its Applications*, 359(1-4):289–305, 2006.
 - [3] I. Borazjani and F. Sotiropoulos. Numerical investigation of the hydrodynamics of carangiform swimming in the transitional and inertial flow regimes. *Journal of Experimental Biology*, 211(10):1541–1558, 2008.
 - [4] I. Borazjani and F. Sotiropoulos. Numerical investigation of the hydrodynamics of anguilliform swimming in the transitional and inertial flow regimes. *Journal of Experimental Biology*, 212(4):576–592, 2009.
 - [5] Fabian Bösch, Shyam S Chikatamarla, and Ilya V Karlin. Entropic multirelaxation lattice Boltzmann models for turbulent flows. *Phys. Rev. E*, 92(4):43309, 2015.
 - [6] J Carling, Thelma L Williams, and G Bowtell. Self-propelled anguilliform swimming: Simultaneous solution of the two-dimensional Navier-Stokes equations and Newton’s laws of motion. *Journal of Experimental Biology*, 201(23):3143–3166, 1998.
 - [7] Hudong Chen, Satheesh Kandasamy, Steven Orszag, Rick Shock, Sauro Succi, and Victor Yakhot. Extended Boltzmann Kinetic Equation for Turbulent Flows. *Science*, 301(5633):633–636, 2003.

- [8] Jian-Yu Cheng, Li-Xian Zhuang, and Bing-Gang Tong. Analysis of swimming three-dimensional waving plates. *Journal of Fluid Mechanics*, 232:341–355, 1991.
- [9] S.S. Chikatamarla and I. V. Karlin. Entropic lattice Boltzmann method for turbulent flow simulations: Boundary conditions. *Physica A*, 392(9):1925–1930, 2013.
- [10] M. D. De Tullio, a. Cristallo, E. Balaras, and R. Verzicco. Direct numerical simulation of the pulsatile flow through an aortic bileaflet mechanical heart valve. *Journal of Fluid Mechanics*, 622:259, 2009.
- [11] B. Dorschner, S.S. Chikatamarla, F. Bösch, and I.V. Karlin. Grad’s approximation for moving and stationary walls in entropic lattice Boltzmann simulations. *Journal of Computational Physics*, 295: 340–354, aug 2015.
- [12] B. Dorschner, F. Bösch, S.S. Chikatamarla, K. Boulouchos, and I.V. Karlin. Entropic Multi-Relaxation Time Lattice Boltzmann Model for Complex Flows. *Journal of Fluid Mechanics*, 801: 623–651, 2016.
- [13] B. Dorschner, N. Frapolli, S.S. Chikatamarla, and I.V. Karlin. A block-structured grid refinement technique for entropic lattice Boltzmann models. *submitted to Phys. Rev. E*, 2016.
- [14] G. Eitel-Amor, M. Meinke, and W. Schröder. A lattice-Boltzmann method with hierarchically refined meshes. *Computers and Fluids*, 75:127–139, 2013.
- [15] Orjan Ekeberg. A combined neuronal and mechanical model of fish swimming. *Biological Cybernetics*, 69(5-6):363–374, 1993.
- [16] N. Frapolli, S. S. Chikatamarla, and I. V. Karlin. Multispeed entropic lattice Boltzmann model for thermal flows. *Physical Review E*, 90(4):043306, 2014.
- [17] N. Frapolli, S. S. Chikatamarla, and I. V. Karlin. Entropic lattice Boltzmann model for compressible flows. *Physical Review E*, 92(6):061301, 2015.
- [18] Martin Geier, Andreas Greiner, and Jan G. Korvink. Cascaded digital lattice Boltzmann automata for high Reynolds number flow. *Physical Review E*, 73(6):066705, 2006.
- [19] Alexander N. Gorban and Iliya V. Karlin. *Invariant Manifolds for Physical and Chemical Kinetics*, volume 660. Springer, Lect. Notes Phys, 2004. ISBN 3642061532.
- [20] B Y J Gray. Studies in animal locomotion III. *Journal of Experimental Biology*, (3):386–400, 1933.
- [21] F. Hess and J. J. Videler. Fast Continuous Swimming of Saithe (*Pollachius Virens*): A Dynamic Analysis of Bending Moments and Muscle Power. *Journal of Experimental Biology*, 109(1):229–251, 1984.
- [22] Robert Howell, Ning Qin, Jonathan Edwards, and Naveed Durrani. Wind tunnel and numerical study of a small vertical axis wind turbine. *Renewable Energy*, 35(2):412–422, 2010.
- [23] Auke Jan Ijspeert and Jérôme Kodjabachian. Evolution and Development of a Central Pattern Generator for the Swimming of a Lamprey. *Artificial Life*, 5(3):247–269, 1999.
- [24] T. A. Johnson and V. C. Patel. Flow past a sphere up to a Reynolds number of 300. *Journal of Fluid Mechanics*, 378:19–70, 1999.
- [25] I. V Karlin, A Ferrante, and H. C Öttinger. Perfect entropy functions of the Lattice Boltzmann method. *Europhysics Letters*, 47(2):182–188, 1999.
- [26] I V Karlin, F Bösch, and S S Chikatamarla. Gibbs’ principle for the lattice-kinetic theory of fluid dynamics. *Physical Review E*, 90(3):31302, 2014.
- [27] S. Kern and P. Koumoutsakos. Simulations of optimized anguilliform swimming. *Journal of Experimental Biology*, 209(24):4841–4857, 2006.
- [28] Pierre Lallemand and Li-Shi Luo. Theory of the lattice Boltzmann Method: Dispersion, Dissipation, Isotropy, Galilean Invariance, and Stability. *Physical Review E*, 61(6):6546–6562, 2000.
- [29] Jonas Latt and Bastien Chopard. Lattice Boltzmann method with regularized pre-collision distribution functions. *Mathematics and Computers in Simulation*, 72(2-6):165–168, 2006.
- [30] M. J. Lighthill. Note on the swimming of slender fish. *Journal of Fluid Mechanics*, 9(02):305, 1960.
- [31] M J Lighthill. Hydromechanics of aquatic animal propulsio. *Annual Review of Fluid Mechanics*, 1 (1):413–446, 1969.
- [32] M. J. Lighthill. Aquatic animal propulsion of high hydromechanical efficiency. *Journal of Fluid Mechanics*, 44(02):265, 1970.
- [33] M. J. Lighthill. Large-Amplitude Elongated-Body Theory of Fish Locomotion. *Proceedings of the Royal Society of London B: Biological Sciences*, 179(1055):125–138, 1971.
- [34] L. G. Margolin, W. J. Rider, and F. F. Grinstein. Modeling turbulent flow with implicit LES. *Journal of Turbulence*, 7(15):N15, 2006.

- [35] Len G. Margolin and William J. Rider. A rationale for implicit turbulence modelling. *International Journal for Numerical Methods in Fluids*, 39(9):821–841, 2002.
- [36] A M Mazloomi, S S Chikatamarla, and I V Karlin. Entropic Lattice Boltzmann Method for Multiphase Flows. *Physical Review Letters*, 114(17):174502, 2015.
- [37] Gregory McGowan, Ashok Gopalarathnam, Michael Ol, Jack Edwards, and Daniel Fredberg. Computation vs. Experiment for High-Frequency Low-Reynolds Number Airfoil Plunge. *AIAA paper*, 653:2008, 2008.
- [38] M Mendoza, B M Boghosian, H J Herrmann, and S Succi. Fast Lattice Boltzmann Solver for Relativistic Hydrodynamics. *Physical Review Letters*, 105:014502, 2010.
- [39] Ulrike K Müller, Joris Smit, Eize J Stamhuis, and John J Videler. How the body contributes to the wake in undulatory fish swimming. *Journal of Experimental Biology*, 204(16):2751–2762, 2001.
- [40] Manjusha Namburi, Siddharth Krithivasan, and Santosh Ansumali. Crystallographic Lattice Boltzmann Method. *Scientific reports*, 6:27172, 2016.
- [41] K Ou, P Castonguay, and A Jameson. 3D Flapping Wing Simulation with High Order Spectral Difference Method on Deformable Mesh. *49th AIAA Aerospace Sciences Meeting including the New Horizons Forum and Aerospace Exposition*, (January), 2011.
- [42] C S Peskin. Numerical analysis of blood flow in the heart. *Journal of Computational Physics*, 25(3):220–252, 1977.
- [43] Amanda Elizabeth Randles. *Modeling Cardiovascular Hemodynamics Using the Lattice Boltzmann Method on Massively Parallel Supercomputers*. PhD thesis, 2003.
- [44] Martin Schmitt, Christos E. Frouzakis, Ananias G. Tomboulides, Yuri M. Wright, and Konstantinos Boulouchos. Direct numerical simulation of multiple cycles in a valve/piston assembly. *Physics of Fluids*, 26(3):035105, 2014.
- [45] Kosuke Suzuki and Takaji Inamuro. Effect of internal mass in the simulation of a moving body by the immersed boundary method. *Computers and Fluids*, 49(1):173–187, 2011.
- [46] Eric D Tytell. The hydrodynamics of eel swimming II. Effect of swimming speed. *Journal of experimental biology*, 207(19):3265–3279, 2004.
- [47] Eric D Tytell and George V Lauder. The hydrodynamics of eel swimming: I. Wake structure. *Journal of Experimental Biology*, 207(11):1825–1841, 2004.
- [48] Miguel R. Visbal. High-Fidelity Simulation of Transitional Flows past a Plunging Airfoil. *AIAA Journal*, 47(January):2685–2697, 2009.
- [49] Binghai Wen, Chaoying Zhang, and Haiping Fang. Hydrodynamic Force Evaluation by Momentum Exchange Method in Lattice Boltzmann Simulations. *Entropy*, 17(12):8240–8266, 2015.
- [50] Th Yao-Tsu Wu. Hydromechanics of swimming of fishes and cetaceans. *Advances in Applied Mechanics*, 11:1–63, 1971.